analytical chemistry

Article

Cite This: Anal. Chem. 2019, 91, 7712−7718

pubs.acs.org/ac

Stand-off Hyperspectral Raman Imaging and Random Decision Forest Classification: A Potent Duo for the Fast, Remote Identification of Explosives

Christoph Gasser, Michael Göschl, Johannes Ofner, and Bernhard Lendl*

Institute of Chemical Technologies and Analytics, TU Wien, Getreidemarkt 9/164, 1060 Vienna, Austria

Supporting Information

ABSTRACT: In this study, we present a stand-off hyperspectral Raman imager (HSRI) for the fast detection and classification of different explosives at a distance of 15 m. The hyperspectral image cube is created by using a liquid crystal tunable filter (LCTF) to select a specific Raman shift and sequentially imaging spectral images onto an intensified CCD camera. The laser beam is expanded to illuminate the field of view of the HSRI and thereby improves large area scanning of suspicious surfaces. The collected hyperspectral image cube (HSI) is evaluated and classified using a random decision forest (RDF) algorithm. The RDF is trained with a training set of mg-amounts of different explosives, i.e., TNT, RDX, PETN, $NaClO_3$, and NH_4NO_3, on an artificial aluminum substrate. The resulting classification is validated, and variable importance is used to optimize the RDF using spectral descriptors, effectively reducing the dimensionality of the data set. Using the gained information, a faster acquisition and calculation mode can be designed, giving improved results in classification at a much higher repetition rate.

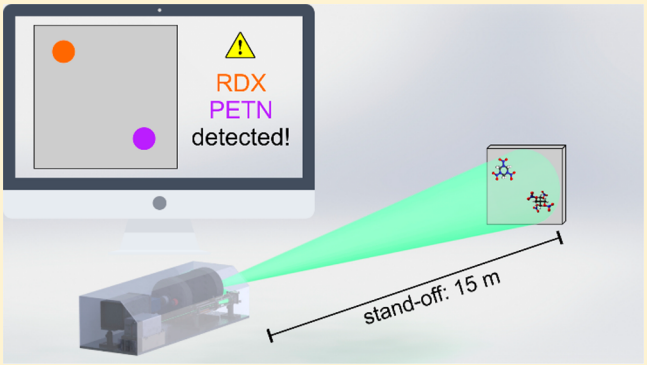

The advance in computer or machine vision over the last decades fueled a wide range of new and exciting possibilities for automated recognition, classification, and control in medical,[1,2] industrial,[3,4] as well as military[5] areas. At the same time, the need of rapid detection of localized traces of harmful substances, such as explosives, at safe distances increased due to the rise of domestic attacks and the accompanying elevated security risk and screenings. It is imperative, then, to distinguish the chemical composition of a target substance in an area of interest, deciding whether or not it poses a threat. This can most effectively be done by adding another layer of information to an ordinary image by means of spectroscopy, a technique known as hyperspectral imaging (HSI). Continuous advancements in instrumentation led to a plethora of different combinations of spectroscopic and imaging techniques with the goal of creating spatially resolved chemical maps for various different applications, ranging from food quality and safety analysis[6] to biomedical engineering.[7] Raman spectroscopy (RS) seems to be particularly suited as a spectroscopic technique to be implemented in such HSI screening devices, since it offers high chemical selectivity, while being a nondestructive method, and features the ability to be used at remote distances due to its scattering nature. Lasers allow light to be transported over significant distances without high losses; hence, probing distant samples via stand-off RS is viable. In stand-off RS applications, the instrument is physically separated from the sample,[8] which is especially useful if dangerous or harmful substances are the target of an investigation, or the target area is poorly accessible. The detection of explosives and explosive residues using stand-off RS became prominent due to the successful endeavor of this kind of instruments to detect tiny amounts of explosive material at significant distances, shown in several studies over the last years.[9−11] The result of a hyperspectral image (HSI) experiment is a data cube, where two axes represent the local information, and an additional axis is occupied by the spectral variables. Most spectroscopic techniques are suitable for obtaining HSI, generally the recording mechanism can be divided into three techniques, whiskbroom,[12] pushbroom,[13] and staring or spectral scanning[14] measurement. The whiskbroom scanner uses a single point detection scheme, which mapped over a certain area produces the HSI. The first RS HSI instruments were based on this scheme using microscope systems, where the implementation of RS due to its scattering nature and ability to work in the visible spectral range is preferable.[15] High spatial resolution is a direct benefit of using an optical microscope as both excitation and collection optic, which can even dissect samples optically into μm thin slices when a confocal arrangement is used.[16] Similarly, in the pushbroom approach, a line is scanned over an area of interest with an array detector, where one axis is

Received: February 18, 2019
Accepted: May 13, 2019
Published: May 13, 2019

DOI: 10.1021/acs.analchem.9b00890
Anal. Chem. 2019, 91, 7712−7718

Table 1. Results of the RDF Classifiers for the Different Explosive Classes[a]

	OOB average error in %							
	$NaClO_3$	NH_4NO_3	PETN	RDX	TNT	# var.	meas. time	calc. time
RDF1	1.44	1.82	7.82	5.94	3.67	768	51 min 15 s	3
RDF2	0.37	0.85	5.2	2.63	1.1	80	5 min 20 s	1

[a]Calculation time is given as a relative number.

dedicated to the spectral axis.[17] Lastly, the staring or spectral scanning techniques utilize a tunable filter to select a specific spectral feature and acquire an image. The HSI is built by consecutively stacking spectral images. The first implementation again employed microscopes in combination with acusto-optical (AOTFs) and liquid crystal tunable filters (LCTFs).[18]

Recently, even Bragg tunable filters have been used in Raman microspectroscopy.[19] A comparison of all techniques of hyperspectral raman imaging (HSRI) was performed by Schlücker et al.[20] Regarding stand-off HSRI instruments, most are designed as whiskbroom imagers and are therefore of limited use when large areas should be investigated, but mapping of the excitation laser over the whole area is a tedious process. Pushbroom systems have been tested as stationary screening devices.[17] Staring or spectral scanning stand-off Raman imagers have been proposed and tested over the past years,[21] where the dispersive element is a tunable filter with a large enough aperture to transmit the whole field-of-view (FOV) of the collecting optic as an image directly onto the detector array. Here, LCTFs can facilitate narrow bandpass filters suitable for RS, which can be tuned electronically in a fast and reliable manner, while on a small footprint. In combination with a suitable intensified CCD (iCCD) camera and a small, air-cooled, pulsed laser, it is possible to design a stand-off HSRI system, which can be field deployable. The limitation of the LCTFs is the usable spectral range, especially regarding the UV region, where the absorbance of the incorporated materials in LCTFs hinders their application. Hence, recently, custom built tunable filters based on Fabry–Pérot interferometers have been studied as viable alternatives for UV excitation.[22] These are, however, still not available commercially..

The resulting HSI data sets are usually highly dimensional and complex, challenging even experts with their evaluation. Therefore, chemometric algorithms found their way into the field of RS as handy tools for breaking down thousands of complex spectra into digestible information.[23] In regards to detection of explosives, a fast and robust classification of the obtained HSRI would result in easily understandable false color images, which can be also interpreted by trained nonexperts. Here, we propose the usage of a random forest classifier (RDF), due to its ability to perform high quality classification with efficient use of processing power.[24] The RDF consist of an ensemble of decision trees, which are trained by randomly selecting and using a subset of the available data set (defined by the ratio R, in-bag samples), thus growing into a forest of user-defined size (N_T). Classification is reached by majority vote of the class assignment probabilities of each tree, which carry low bias and high variance due to the random pick of samples during training.[25] A major advantage represents the use of the previously left out subset as internal cross-validation on the performance of the RDF by calculating an error estimate known as an out-of-bag (OOB) error (Table 1).[26] Similarly, this can be exploited to investigate on the variable importance (VIP). When comparing OOB errors from the trained RDF with OOB errors from RDFs with randomly permutated sample variables, the effect of each variable can be assessed. This is a useful tool in decreasing the dimensionality of the obtained data, while keeping quality classification.[27]

This results in a considerable reduction of measurement time, especially for the staring HSRI system, as the amount of spectral images to be acquired as the time-consuming step can be reduced significantly.

In this study we present an air-cooled, mobile stand-off HSRI system in the visible spectral range. Accidental detonation or photodegradation of the sample was avoided by using an excitation laser with low pulse energies, but high repetition rates with a defocused beam to illuminate an area corresponding to the field of view of the collection optics. The HSRI works in staring or spectral scanning mode, where an LCTF is used to discriminate a certain Raman shift and collect the image. Different explosive materials are measured at a distance of 15 m. The obtained HSI is the basis to train an RDF, which is used to identify the most important variables and create designated spectral descriptors (SPDCs),[28] reducing the dimensionality of the data set and subsequently improving measurement and calculation time. A second RDF is trained using these SPDCs, showing improved performance, while highlighting the benefits of the synergy between stand-off HSRI and RDF classification for the fast, remote detection of explosives.

MATERIALS AND METHODS

Stand-off Hyperspectral Raman Imager. The direct stand-off imager (Figure 1a) used an air-cooled, Q-switched,

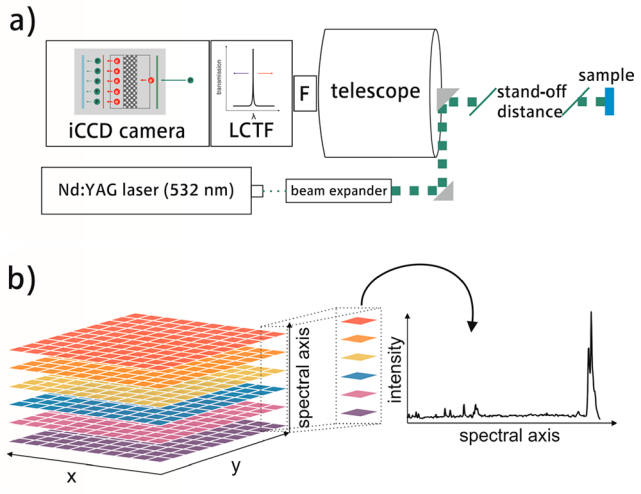

Figure 1. (a) Illustration of the optical setup. The beam emitted by the laser (532 nm, Nd:YAG) is expanded in order to illuminate the field of view of the telescope at the stand-off distance. The Raleigh line is filtered by an edge filter (F), before a tunable liquid crystal filter (LCTF) selects a Raman shift for the spectral image. The image is taken by an iCCD camera synchronized to the pulsed laser output. (b) Sketch of the structure of the resulting hyperspectral image cube.

DOI: 10.1021/acs.analchem.9b00890
Anal. Chem. 2019, 91, 7712−7718

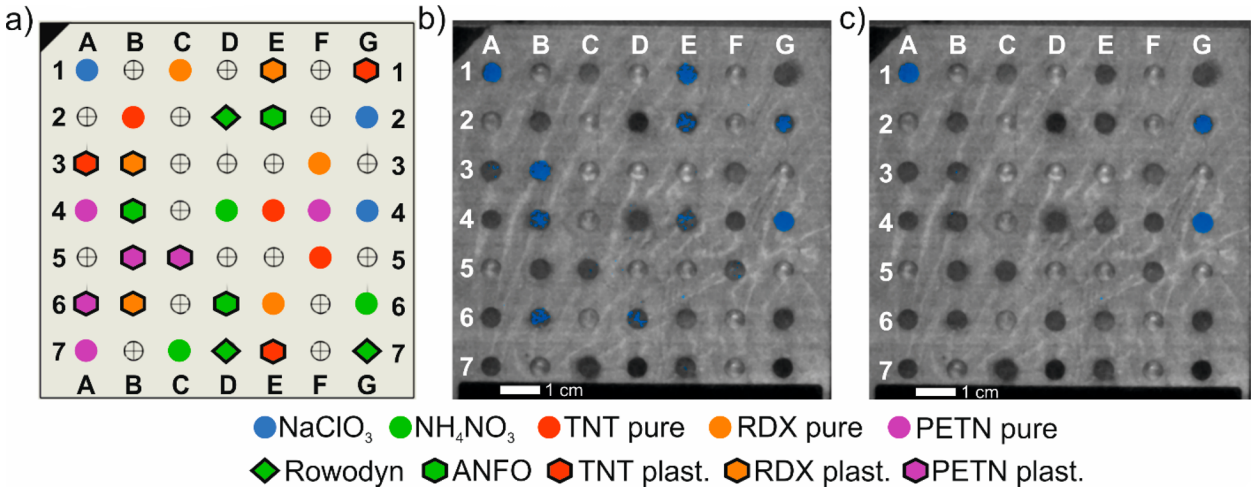

Figure 2. (a) Illustration of the randomly chosen and filled positions of each sample on the sample holder. (b) Overlay of the intensity of the spectral image at 941 cm^{-1} corresponding to the symmetric stretch vibration of $NaClO_3$ on a greyscale image of the sample. (c) Overlay of the intensity of a correlation to a template triangle as the spectral descriptor for the band associated with $NaClO_3$ on a greyscale image of the sample.

frequency-doubled (532 nm) Nd:YAG Explorer One (EONE 532−200, Spectra-Physics, USA) laser with a Gaussian beam profile and adjustable pulse energies ranging from 30 to 300 μJ and repetition rates from single shot to 60 kHz. The laser beam was expanded using a defocused Galilean type beam expander to a diameter of approximately 100 mm at the stand-off distance of 15 m. The backscattered Rayleigh photons were eliminated using a long pass filter (LP03-532RE, Semrock, USA). Afterward, a specific Raman shift was selected using a tunable LCTF filter (VariSpec VISR, PerkinElmer, USA) with a spectral resolution of 0.25 nm and directly imaged onto an iCCD equipped with a quadratic sensor (PIMAX 4 1024f-HBf iCCD, 1024 × 1024 pixels, 13 μm pixels). The spectral images were stacked in order to build the hyperspectral data cube as depicted in Figure 1b. This process was automated using LabVIEW (National Instruments, USA).

Chemicals. *Explosives.* An appropriate rectangular sample holder in aluminum with an edge length of 80 mm was designed. Then, 49 wells with a diameter of 4 mm and a depth of 1 mm were cut into the aluminum, acting as a holder for the explosives. The wells were randomly filled with 10 mg of the different available explosives or precursors so that every class was represented three times (Figure 2a). Three pure explosive components, trinitrotoluene (TNT), pentaerythritol tetranitrate (PETN), and 1,3,5-trinitro-1,3,5-triazinane (research department explosive, RDX), were used in this study. At the same time, the three pure components were also added as plastic variants, i.e., the pure explosives with added binders, desensitizers, waterproof coatings, and plasticizers, which help increase their usability and storability.[29] Rowodyn is a commercially available explosive, mostly composed of NH_4NO_3, nitroglycerine, ethylene glycol dinitrate, and fuel. Ammonium nitrate fuel oil (ANFO) is a mixture of NH_4NO_3 and fuel oil. All these samples were acquired from the Austrian Armed Forces. Finally, $NaClO_3$ and NH_4NO_3 were acquired from Sigma-Aldrich as examples of explosive substances often found in improvised explosive devices.[30]

Other. A 3 mm thick polytetrafluoroethylene (PTFE) plate was acquired from RS Components GmbH (Austria) as a reference material for the test of the stand-off HSRI.

Measurement Parameters. The sample was placed at a distance of 15 m to the telescope. The repetition rate of the laser was set to 10 kHz emitting pulses with a pulse width of approximately 10 ns and pulse energies of 0.21 mJ, giving an average power of 2.1 W, yielding an average radiant energy of 2.7 $\mu J/cm^2$ and an average irradiance of 26.7 mW/cm^2 due to the widened beam. The laser pulses were synchronized to the gate of the intensifier of the iCCD in order to maximize Raman signal and suppress ambient light. The gate of the camera was set to 10 ns to coincide with the laser pulse width. Signal to noise was improved by accumulating 30.000 pulses on the CCD per spectral image, resulting in a total measurement time of 3 s per image. HSI cubes were started at 800 cm^{-1} and ended at 3101 cm^{-1} Raman shift with a spectral image every 3 cm^{-1}, resulting in 768 different spectral layers.

Reference Raman spectra of all components were measured using a confocal Raman microscope (Horiba LabRAM HR, Japan) equipped with frequency-doubled Nd:YAG (532 nm) laser with 20 mW, a 20× objective, 2 s integration time, 10 accumulations, and a grating of 300 gr/mm.

RDF. In order to train the RDF,[25,26] a list of training data points was created. Then, 40 pixels with pure explosives (TNT, PETN, RDX, $NaClO_3$, and NH_4NO_3) were selected manually and associated to their respective class. Preprocessing of the data set included spike removal and baseline correction using Eiler's method[36] over 15 iterations with a smoothness of 10 000 and an asymmetry of 0.001. First, an RDF was trained with all the spectral images as input variables (RDF1). The ratio (R) between used and unused samples (in-bag and out-of-bag OOB samples) was optimized by computing several forests and choosing the ratio which yielded the lowest OOB average errors. Similarly, the optimal number of trees (N_T) was established. Afterward, a feature selection was done via the variable importance of each class. Spectral descriptors, in this case, correlation to a template triangle peak (TC descriptor), were chosen as the new input. The second RDF was trained using those as input variables (RDF2). Both classifications are compared regarding their classification and OOB errors. All calculations were performed using ImageLab (Epina GmbH, Austria).

RESULTS AND DISCUSSION

To assess the capability of the stand-off HSRI to produce quality HSIs (single pixel spectra) over the whole FOV, a PTFE plate

DOI: 10.1021/acs.analchem.9b00890
Anal. Chem. 2019, 91, 7712−7718

was placed at a distance of 15 m and imaged starting at 680–1500 cm^{-1} with steps of 3 cm^{-1}. An acquired single pixel example spectra is displayed in Figure 3a and compares correctly

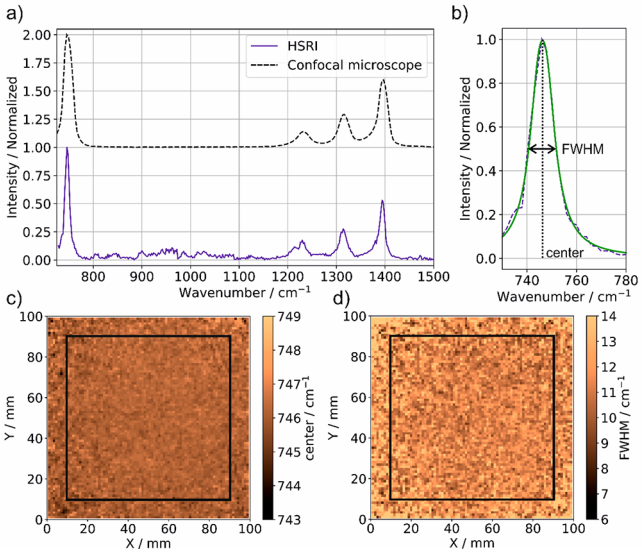

Figure 3. (a) Sample spectra of PTFE compared to a reference measurement using a confocal Raman microscope. (b) Illustration of the curve fit of the band at 746 cm^{-1} with a pseudo-Voigt profile (green curve). (c) Distribution of the center position of the fitted band over the FOV of the HSRI. (d) Distribution of the fwhm of the fitted band over the FOV of the HSRI.

to the given reference spectrum. An important factor for correct and accurate interpretation of the obtained HSI is the wavelength stability of the dispersive element, in this case, the LCTF filter, over the whole FOV. The band of PTFE at 746 cm^{-1} corresponding to the skeletal stretch[37] was chosen because of its high intensity and narrow line width for an in-depth analysis of the stability and accuracy of the LCTF as wavelength discriminator. Both center position and full width at half-maximum (fwhm) of the band were assessed by fitting the band with a pseudo-Voigt profile,[38] as shown in Figure 3b, and extracting the respective parameters. Due to low intensities at the edges of the image because of the Gaussian beam profile, only values inside the rectangular indicated in Figure 3c,d were taken for further analysis, as this was also the size of the test sample. The median center position was found to be 746.2 cm^{-1} with a standard deviation of 0.3 cm^{-1}. The median fwhm was located at 11.3 cm^{-1} with a standard deviation of 0.8 cm^{-1}. Both parameters are well within the specifications of the LCTF and exhibit no drift or inconsistencies over the whole FOV. This is crucial for the device to act as reliable dispersive element in this HSRI application.

The capability to detect the amounts of explosives put into the sample holder at a distance of 15 m is shown exemplary in Figure 4, where raw single pixel spectra chosen from the respective sample positions are compared against reference spectra obtained via measurement using a Raman microscope. The pure components $NaClO_3$ and NH_4NO_3 show quality spectra (Figure 4a,b) both when measured with the stand-off HRSI and the Raman microscope. Analogously, the spectra of RDX and TNT are in good agreement with the respective reference spectrum. Both components exhibit an elevated background, which can be attributed to fluorescence. This leads to fluctuating baseline features (e.g., between 2500 and 2800 cm^{-1} in Figure 4d), which are not sample related and are caused by the transmission characteristics of the Rayleigh edge filter used to block the incoming laser light. The main difference in the spectra obtained with the HSRI and the Raman microscope is the signal-to-noise ratio (SNR). It is higher for the reference spectra, due to the longer integration time and significantly higher incident irradiance when using the microscope. At 532 nm, a 20×

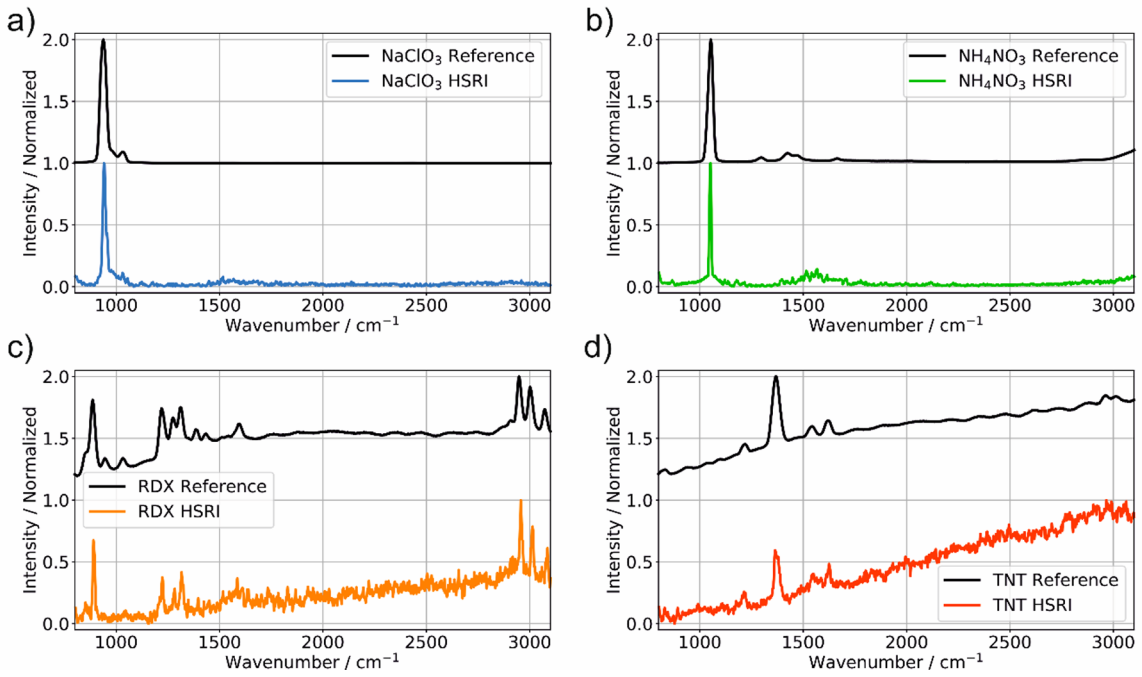

Figure 4. Reference spectra of (a) $NaClO_3$, (b) NH_4NO_3, (c) RDX, and (d) TNT (black curves) obtained via confocal Raman microscope compared to the spectrum of a pixel recorded with the stand-off HSRI at a distance of 15 m. These spectra are not preprocessed, except normalization.

DOI: 10.1021/acs.analchem.9b00890
Anal. Chem. 2019, 91, 7712–7718

objective (NA = 0.4) on a confocal microscope system gives a theoretical spatial resolution of approximately 500 nm. Assuming an area of that diameter, the irradiance under the microscope amounts to 10^{10} mW/cm^2, an increase of approximately 8 orders of magnitude compared to the irradiance of the widened beam. Given that the intensity of a Raman signal is direct proportional to the impinging laser intensity onto the sample, it speaks for the throughput and detectivity of the stand-off HSRI to still show acceptable spectra, even at stand-off distances.

To build an able classifier, the first step taken in this study was to train an RDF classifier (RDF1) using the baseline-corrected intensities of each spectral image as input variables. The training set included 200 reference points per pure class of explosive, manually selected from the 3 possible positions on the sample (Figure S1). To select an optimal R (0.66) and N_T (50), a scan for both parameters was performed, taking the OOB average error as the indicating measure for when optimal classification is reached (Figures S2−S5).

The results of RDF1 are shown in Figure 5a,b. The confusion matrix shows that the training set can be distinguished without any false positives or false negatives. However, the OOB errors reveal differences in the quality of classification between the different explosives. NH_4NO_3 and $NaClO_3$ are better characterized than the other pure components, which is feasible, because of their strong, single standing spectral features. An even more differentiated image is given in Figure 5b, where the RDF1 classifier is applied to the whole data set. Here, various misclassifications can be identified, with sample position B3 showing the biggest error. On this spot, pixels classified as TNT, RDX, and $NaClO_3$ neighbor each other; whereas B3 was prepared with plasticized RDX. Aggregations of false classification on positions with fluorescent samples, like E1, E2, B3, B4, B6, and C5, are also found. The evidence is hardened when Figure 2a,b is compared. Even after baseline correction, the intensity distribution of the band of $NaClO_3$ at 941 cm^{-1} (Figure 2b) does not only cover the areas A1, G2, and G4, as prepared, but also, e.g., B3, B4, B6, and E2. It is apparent that another tool which gives a more selective measure for the abundance of the respective compound has to be found. This challenge was approached by first evaluating the VIP scores of every class when all variables are used, i.e., the VIP scores of RDF1. Figure 6a,b depicts the VIP scores and the respective spectra from a pure pixel for two selected classes, namely, sodium chlorate and TNT. High VIP scores for RDF1 for sodium chlorate are situated around the maximum band intensity at 941 cm^{-1}, which was expected. For TNT the same situation is true with the highest VIP score around the main band associated with the symmetric stretch of the NO_2 at 1361 cm^{-1}, albeit the presence of other bands.

Similarly, it was found that, for all other classes, one spectral feature was predominantly represented in the VIP scores. This spurred the idea of using these small parts of the spectrum for

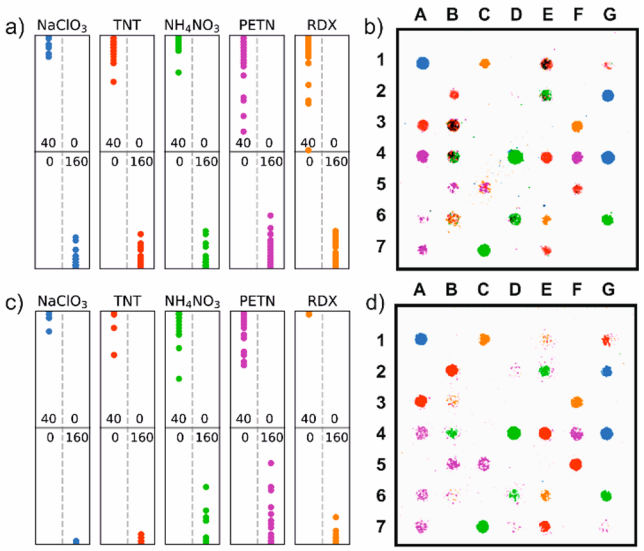

Figure 5. (a) Confusion matrix for the training data set of the RDF1 classification, when all acquired intensities are used as variable (b) RDF1 classifiers with all variables applied over the whole sample, each class is color-coded. (c) Confusion matrix for the training data set of the RDF2, when only the spectral descriptors are used. (d) RDF2 classifier with only spectral descriptors applied over the whole sample, each class is color-coded.

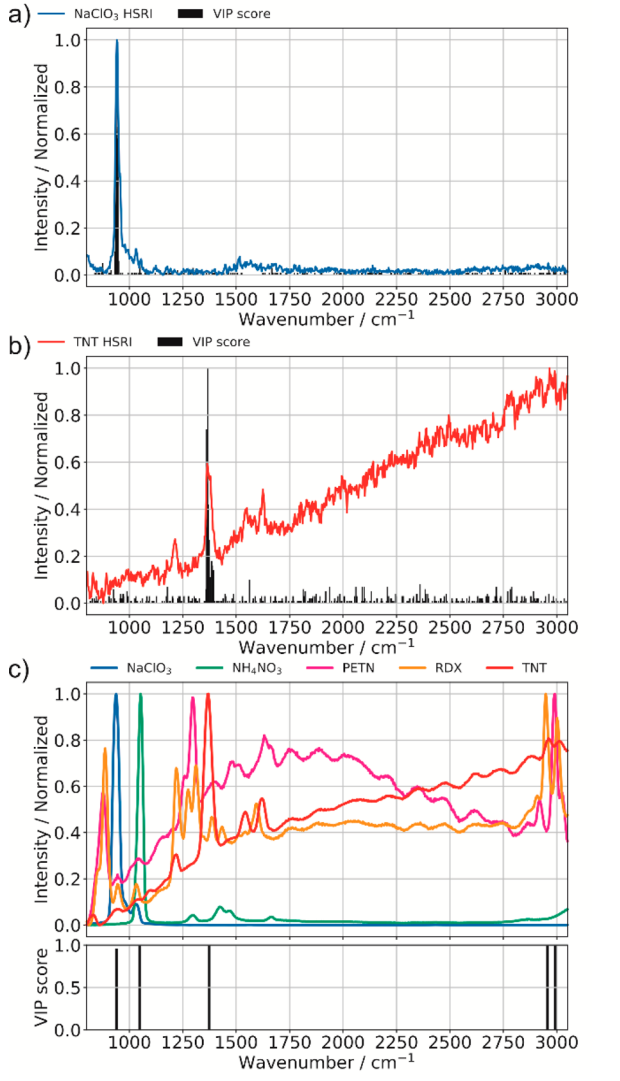

Figure 6. (a) Variable importance (VIP) scores of the $NaClO_3$ class for the RDF using all spectral images as variables. (b) VIP scores of the TNT class for the RDF using all spectral images as variables. (c) VIP scores of all explosive classes for the RDF using only spectral descriptors as variables.

DOI: 10.1021/acs.analchem.9b00890
Anal. Chem. 2019, 91, 7712−7718

classification. However, the fact that elevated baselines with heavy fluorescent backgrounds (e.g., RDX, as shown in Figure 7)

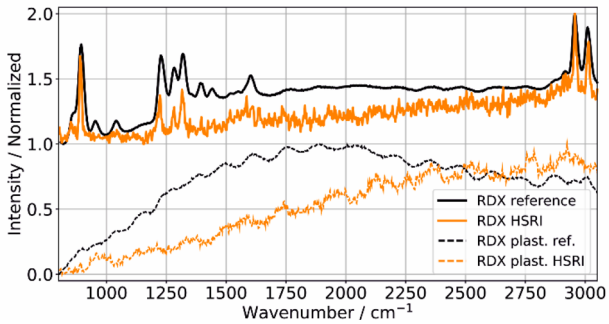

Figure 7. Reference (black, solid line) and stand-off HRSI (orange, solid line) spectra of pure RDX compared to a reference (black, dashed line) and HSRI (orange, dashed line) spectrum of RDX with plasticizer.

heavily affected pure intensities, another spectral descriptor less prone to noise was needed to describe band intensity. Here, a TC descriptor was used. The descriptor is characterized by a triangle template with the parameters b1 and b2 as baseline points and c as center point. The strength of the descriptor is calculated by the positive significant correlation (significance level 0.01) to the data points within the chosen range multiplied by the baseline corrected integral as a measure of band intensity.[39] This descriptor tends to be less sensitive to noise, since for noise, it is unlikely to produce a significant correlation to the triangle template. In comparison to Figure 2b,c, the effect of choosing a TC descriptor with appropriate parameters (Table 2) for sodium chlorate is clearly visible. The TC descriptors

Table 2. Associated Band (Labeled as Band) of the Different Classes of Explosives, Their Band Assignment (Assign), and a Respective Reference[a]

			spectral descriptor: TC		
class	band	assign	c	b1	b2
$NaClO_3$	940[31]	ν^s ClO_3^-	941	917	959
NH_4NO_3	1044[32]	ν^s NO_3^-	1045	1031	1062
PETN	2987[33]	ν^s CH_2	2993	2976	3017
RDX	2959[34]	ν^{as} CH	2957	2939	2978
TNT	1356[35]	ν^s NO_2	1361	1331	1407

[a]Parameters of the triangle correlation (TC) spectral descriptor (c means center; b1 and b2 are baseline points 1 and 2, respectively) used in this study for every class. All numbers have the unit cm^{-1}.

intensity is only observable for the prepared $NaClO_3$ positions, instead of also highlighting points with highly fluorescent backgrounds. The TC descriptor was subsequently also applied to all other regions where the RDF1 gave high VIP scores for the different classes. This resulted in 5 different TC descriptors for the 5 explosive classes investigated in this study, which are summarized in Table 2. Now, the same parameters as in RDF1 were taken to train a second RDF, RDF2, except for the input variables, which, in the case of RDF2, consisted of the five TC descriptors. An R and N_T scan revealed similar behavior of this RDF, so the same values as in RDF1 were used. Again OOB errors were calculated and show an overall improved performance of the classifier (Table 1). Especially, the detection and recognition of sodium chlorate profited from the new spectral descriptors, as was discussed before comparing Figure 2b,c, but is confirmed by the OOB errors found in RDF1 and RDF2. Overall, the OOB errors are reduced for all classes of explosives, which, in turn, results in a much cleaner assessment of the whole sample, when the RDF2 is applied to the whole FOV imaged by the HSRI, shown in Figure 5d.

CONCLUSION

A stand-off hyperspectral Raman imager working at a 532 nm excitation wavelength with a 15 m distance to the sample position was designed, constructed, and tested for its capability to produce quality spectra at low laser irradiance at the target. The stability and correctness of the produced spectra were assessed for every pixel in the FOV of the imager. Different types of explosive samples, namely, ammonium nitrate, sodium chlorate, PETN, RDX, and TNT, were prepared in the mg-range on an aluminum substrate. Additionally, plasticized variants of the explosives as well as a commercial explosive (Rowodyn) were prepared on the same substrate and measured at 15 m. Two RDFs were trained. The first RDF (RDF1) was trained by using all the available pixel intensities of all spectral images of a defined test set. With the help of the variable importance in RDF1, TC descriptors for the pure components in the test set were constructed and used in the training of a second RDF (RDF2). Both RDFs were compared regarding their out-of-bag errors and classification performance of the whole sample. It is shown, that the TC spectral descriptor can significantly increase the selectivity and specificity of the signal response and therefore improve the classification prowess of the RDF. Additionally, since for the TC descriptor fewer spectral positions are needed, the measurement time decreases by a factor of 10, while the computation time is reduced by a factor of 3 due to the reduction of variables. Fluorescence remains a challenge in this spectral region, possible solutions include moving the excitation either to the near-infrared or to deep UV wavelengths[40] or use of faster gating to discriminate fluorescence in the time domain.[41] In conclusion, we show that the combination of direct HSRI and RDF with an improved selection of spectral descriptors enable a fast large area detection of mg-amounts of explosives at a distance of 15 m using Raman spectroscopy in the visible regime.

ASSOCIATED CONTENT

Supporting Information

The Supporting Information is available free of charge on the ACS Publications website at DOI: 10.1021/acs.analchem.9b00890.

Prepared sample positions with the different explosives, manually selected sample positions for the RDF training data set, OOB average error in dependence of the selected in-bag to OOB ratio for RDF1, OOB average error in dependence of the selected forest size (N_T) for RDF1, OOB average error in dependence of the selected in-bag to OOB ratio for RDF2, and OOB average error in dependence of the selected forest size (N_T) for RDF2 (PDF)

AUTHOR INFORMATION

Corresponding Author

*E-mail: bernhard.lendl@tuwien.ac.at.

ORCID

Christoph Gasser: 0000-0002-6329-2560

DOI: 10.1021/acs.analchem.9b00890
Anal. Chem. 2019, 91, 7712−7718

Author Contributions

C.G., J.O., and B.L. designed the HSRI prototype and the experiment. C.G. and M.G. did the measurements and evaluated the obtained data set. C.G., J.O., and B.L. wrote the manuscript.

Notes

The authors declare no competing financial interest.

■ ACKNOWLEDGMENTS

Financial support was provided by the Austrian Science Fund (FWF) under the scope of the Translational-Research programme within the research project "Advanced stand-off Raman spectroscopy for chemical identification from safe distances" (TRP-265). The authors thank Prof. Johannes Lohninger for his support while using ImageLab.

■ REFERENCES

(1) Capitán-Vallvey, L. F.; López-Ruiz, N.; Martínez-Olmos, A.; Erenas, M. M.; Palma, A. J. *Anal. Chim. Acta* **2015**, *899*, 23−56.
(2) Opitz, J.; Parsia, B.; Sattler, U. *CEUR Workshop Proc.* **2009**, *529* (5), 858−872.
(3) Yan, T. S.; Cui, D. W. *2006 7th Int. Conf. Comput. Ind. Des. Concept. Des. CAIDC* **2006**, 9487146.
(4) Brosnan, T.; Sun, D. W. *J. Food Eng.* **2004**, *61*, 3−16.
(5) Al-Kaff, A.; Martín, D.; García, F.; Escalera, A.; Armingo, J. M. *Expert Syst. Appl.* **2018**, *92*, 447−463.
(6) Gowen, A. A.; O'Donnell, C. P.; Cullen, P. J.; Downey, G.; Frias, J. M. *Trends Food Sci. Technol.* **2007**, *18* (12), 590−598.
(7) Li, Q.; He, X.; Wang, Y.; Liu, H.; Xu, D.; Guo, F. *J. Biomed. Opt.* **2013**, *18* (10), 100901.
(8) Hobro, A. J.; Lendl, B. *TrAC, Trends Anal. Chem.* **2009**, *28* (11), 1235−1242.
(9) Misra, A. K.; Sharma, S. K.; Acosta, T. E.; Porter, J. N.; Bates, D. E. *Appl. Spectrosc.* **2012**, *66* (11), 1279−1285.
(10) Zachhuber, B.; Ramer, G.; Hobro, A. J.; Lendl, B. *Proc. SPIE* **2010**, *43*, 78380F.
(11) Wallin, S.; Pettersson, A.; Ostmark, H.; Hobro, A. *Anal. Bioanal. Chem.* **2009**, *395* (2), 259−274.
(12) Adão, T.; Hruška, J.; Pádua, L.; Bessa, J.; Peres, E.; Morais, R.; Sousa, J. J. *Remote Sens* **2017**, *9* (11), 1110.
(13) Boldrini, B.; Kessler, W.; Rebner, K.; Kessler, R. W. *J. Near Infrared Spectrosc.* **2012**, *20* (5), 438−508.
(14) Li, Q.; He, X.; Wang, Y.; Liu, H.; Xu, D.; Guo, F. *J. Biomed. Opt.* **2013**, *18* (10), 100901.
(15) Delhaye, M.; Dhamelincourt, P. *J. Raman Spectrosc.* **1975**, *3* (1), 33−43.
(16) Dieing, T.; Hollricher, O.; Toporski, J. Confocal Raman Microscopy. *Springer Series in Optical Sciences*; Dieing, T., Hollricher, O., Toporski, J., Eds.; Springer Berlin Heidelberg: Berlin, 2011; Vol. *158*.
(17) Zachhuber, B.; Östmark, H.; Carlsson, T. *Spatially Offset Hyperspectral Stand-off Raman Imaging for Explosive Detection inside Containers*; Fountain, A. W., Ed.; 2014; p 90730J.
(18) Morris, H. R.; Hoyt, C. C.; Treado, P. J. *Appl. Spectrosc.* **1994**, *48* (7), 857−866.
(19) Gaufrès, E.; Marcet, S.; Aymong, V.; Tang, N. Y. W.; Favron, A.; Thouin, F.; Allard, C.; Rioux, D.; Cottenye, N.; Verhaegen, M.; Martel, R. *J. Raman Spectrosc.* **2018**, *49* (1), 174−182.
(20) Schlücker, S.; Schaeberle, M. D.; Huffman, S. W.; Levin, I. W. *Anal. Chem.* **2003**, *75* (16), 4312−4318.
(21) Östmark, H.; Nordberg, M.; Carlsson, T. E. *Appl. Opt.* **2011**, *50* (28), 5592−5599.
(22) Glimtoft, M.; Bååth, P.; Saari, H.; Mäkynen, J.; Näsilä, A.; Östmark, H. *Towards Eye-Safe Standoff Raman Imaging Systems*; Bishop, S. S., Isaacs, J. C., Eds.; 2014; Vol. *9072*, p 907210.
(23) Ofner, J.; Brenner, F.; Wieland, K.; Eitenberger, E.; Kirschner, J.; Eisenmenger-Sittner, C.; Török, S.; Döme, B.; Konegger, T.; Kasper-Giebl, A.; Hutter, H.; Friedbacher, G.; Lendl, B.; Lohninger, H. *Sci. Rep.* **2017**, *7* (1), 1−11.
(24) Pal, M. *Int. J. Remote Sens.* **2005**, *26* (1), 217−222.
(25) Breiman, L. *Mach. Learn.* **2001**, *45* (1), 5−32.
(26) Cutler, A.; Cutler, D. R.; Stevens, J. R. *Ensemble Machine Learning* **2012**, 157.
(27) Belgiu, M.; Dragut, L. *ISPRS J. Photogramm. Remote Sens.* **2016**, *114*, 24−31.
(28) Ofner, J.; Kamilli, K. A.; Eitenberger, E.; Friedbacher, G.; Lendl, B.; Held, A.; Lohninger, H. *Anal. Chem.* **2015**, *87* (18), 9413−9420.
(29) Meyer, R.; Khler, J.; Homburg, A. *Explosives*; Wiley-VCH Verlag GmbH & Co. KGaA: Weinheim, Germany, 2007.
(30) Kavicky, V.; Figuli, L.; Jangl, S.; Ligasová, Z. *WIT Trans. Built Environ.* **2014**, 297−309.
(31) Bates, J. B. *J. Chem. Phys.* **1971**, *55* (2), 494−503.
(32) Ghosh, M.; Wang, L.; Asher, S. A. *Appl. Spectrosc.* **2012**, *66* (9), 1013−1021.
(33) Gruzdkov, Y. A.; Gupta, Y. M. *J. Phys. Chem. A* **2001**, *105* (25), 6197−6202.
(34) Infante-Castillo, R.; Pacheco-Londoño, L.; Hernández-Rivera, S. P. *Spectrochim. Acta, Part A* **2010**, *76* (2), 137−141.
(35) Daniel, N. W.; Lewis, I. R.; Griffiths, P. R. *Appl. Spectrosc.* **1997**, *51* (12), 1868−1879.
(36) Eilers, P. H. C. *Anal. Chem.* **2003**, *75* (14), 3631−3636.
(37) Peacock, C. J.; Hendra, P. J.; Willis, H. A.; Cudby, M. E. A. *J. Chem. Soc. A* **1970**, 2943.
(38) Sánchez-Bajo, F.; Cumbrera, F. L. *J. Appl. Crystallogr.* **1997**, *30* (4), 427−430.
(39) Lohninger, H.; Varmuza, K. *Anal. Chem.* **1987**, *59* (2), 236−244.
(40) Nagli, L.; Gaft, M.; Fleger, Y.; Rosenbluh, M. *Opt. Mater. (Amsterdam, Neth.)* **2008**, *30* (11), 1747−1754.
(41) Johansson, I.; Zachhuber, B.; Nordberg, M.; Östmark, H. *Proc. SPIE* **2013**, *8710*, 87100R−87100R-8.

DOI: 10.1021/acs.analchem.9b00890
Anal. Chem. 2019, 91, 7712−7718